



# Creep Properties of a Nickel-Based Single Crystal Superalloy with Low Density

Yuling Du<sup>1,2</sup> · Zihao Tan<sup>1</sup> · Yanhong Yang<sup>1</sup> · Xinguang Wang<sup>1</sup> · Yizhou Zhou<sup>1</sup> · Jingguo Li<sup>1</sup> · Xiaofeng Sun<sup>1</sup>

Received: 24 August 2020 / Accepted: 13 October 2020 / Published online: 4 January 2021  
© The Korean Institute of Metals and Materials 2021

## Abstract

A novel nickel-based single crystal superalloy with low density had been designed and the creep deformation mechanisms of the experiment alloy under two conditions (1050 °C/200 MPa and 1100 °C/137 MPa) had been systematically discussed. The topological inversion had been observed after fracture under the above two conditions. The effects of temperature and stress on creep life of the experiment alloy had been found no significant difference under the two conditions. It was indicated that the small decrease in temperature exerted limited influence on the creep behaviors of single crystal superalloys in the range of high temperature.

**Keywords** Nickel-based single crystal superalloy · Creep behavior · Microstructural evolution · Topological inversion

## 1 Introduction

According to the point of engines design, especially for the engine blades, the application of high density alloys will produce large centrifugal stress which may cause the premature fail of the blades [1, 2]. Thus, many researchers have devoted to the design and development of novel low-density single crystal superalloys. The key point of designing the low-density alloy is to reduce the content of high-density refractory elements in the alloy. However, these refractory elements are the root of the SX superalloy which possess high temperature capability of the alloys [3–10]. Therefore, it is a challenge for the researchers who try to skillfully resolve the contradiction between the volume of refractory elements and high temperature capability. In the past decades, a kind of high performance low-density SX superalloy

have been designed through optimizing the ratio of alloying elements, rationalizing the casting process and heat treatments [11–14].

The combination of thermal stress caused by internal cooling and centrifugal stress caused by high-speed rotation is considered as the main stresses which are applied on the turbine blades [15]. Additionally, high temperature also has a significant effect on the microstructural evolution. Thus, the creep damage caused by the superposition of stress and temperature is the main creep failure mechanism of nickel-based single crystal superalloys. It is considered that high temperature creep strength is a basic indicator of mechanical performance for nickel-based SX superalloys [16, 17]. The aim of this work is to preliminarily design a low-density nickel-based single crystal superalloy and systematically analyze the creep behavior under high-temperature and low-stress conditions.

✉ Yuling Du  
yldu18b@imr.ac.cn

✉ Yanhong Yang  
yhyang@imr.ac.cn

✉ Yizhou Zhou  
yzzhou@imr.ac.cn

<sup>1</sup> Institute of Metal Research, Chinese Academy of Sciences, Shenyang 110016, China

<sup>2</sup> School of Materials Science and Engineering, University of Science and Technology of China, Shenyang 110016, China

## 2 Experimental Procedures

In order to meet the requirements of turbine blades for small vortex shaft and turbojet engines, the authors try to design a Re-containing SX superalloy with the combination of low-density and high-strength. In this alloy, 3 wt% rhenium (Re) was added to meet the requirements of high-strength, and 7.5 wt% Chromium (Cr) was adopted to promote the corrosion and oxidation resistance under high temperature

conditions. On the other hand, 7.9 wt% Molybdenum (Mo) + Tungsten (W) + Tantalum (Ta) was added into the alloy in order to meet the requirements of low-density and high temperature strength during extreme conditions. The nominal chemical compositions of the experimental SX superalloy in this work is listed in Table 1. In this work, the experimental alloy is named LD (Low density) single-crystal superalloy.

According to the alloy composition listed in Table 1, the prepared raw materials were melted by Z–G 0.01 type vacuum induction furnace and cast into master alloy ingot. The single crystal bars of the [001] orientation were cast by crystal selection method in a directional solidification vacuum furnace under a high thermal gradient. After that, the as-cast rods were cut to short bars of about 68 mm in length. The heat treatment was carried out on the experimental alloy as follows:

1310 °C/1h + 1320 °C/5h + AC(air cooling) → 1080 °C/5h + AC → 900 °C/8h + AC

In this paper, the density of single crystal superalloy was measured by Archimedes drainage method. The average density value of the alloy is about 8.2 g/cm<sup>3</sup>, which is significantly lower than that of the other typical second-generation Ni-based SX superalloys. The density of several typical second-generation single crystal superalloys is above 8.6 g/cm<sup>3</sup>. For example, the densities of PWA1484 alloy, CMSX-4 alloy, DD6alloy are 8.95 g/cm<sup>3</sup>, 8.70 g/cm<sup>3</sup> and 8.95 g/cm<sup>3</sup> respectively [16].

Creep specimens were then machined from the post-heat treated single crystal bars. The creep specimens have a cylindrical shape with a diameter of 5 mm and a length of 25 mm. Creep deformations were carried out under 1050 °C/200 MPa and 1100 °C/137 MPa at a H-300 creep test machine. Creep fracture of the alloy was analyzed by means of scanning

electron microscopy (SEM) and transmission electron microscopy (TEM). After the creep tests, the foils for transmission electron microscopy (TEM) observation were cut perpendicular to the [001] direction and 5 mm apart from the fracture. These thin foils were electrochemically thinned in a solution of HClO<sub>4</sub>/10 g + C<sub>2</sub>H<sub>5</sub>OH/90 g at a current of 20 mA and temperature of –20 °C. The microstructures of all specimens were examined using a JEM 2100 TEM at 200 kV.

## 3 Results and Discussion

### 3.1 Microstructures in the Post Heat-Treated Conditions

The initial  $\gamma'$  precipitates morphologies of the heat-treated experimental alloy are shown in Fig. 1. It can be clearly

seen that the cubic  $\gamma'$  precipitates are coherently embedded in the  $\gamma$  matrix, and no obvious broadening of the  $\gamma$  matrix channel is observed, which indicates that the two-stage aging heat treatment is reasonable. The statistical analysis of the experimental alloy after the standard heat-treatment (Fig. 1b) shows that the average size of the  $\gamma'$  precipitates is about 0.3  $\mu$ m, the volume fraction is approximately 65 vol%, and the gamma matrix width is about 50 nm.

### 3.2 Creep Curves

In this paper, two conditions (1050 °C/200 MPa and 1100 °C/137 MPa) are selected to test the creep performance of the alloy at high temperature and low stress. Figure 2a and b show the creep curves of the experimental alloy under

**Table 1** Nominal compositions of the LD single crystal superalloy alloy (wt%)

Elements	Cr	Co	Al	Ti	Mo + Ta + W	Re	Hf	Ni
Weight percentage	7.5	7	5	1.0	7.9	3	0.1	68.52

**Fig. 1** SEM picture of  $\gamma/\gamma'$  phases after standard heat treatment and corresponding statistical results of the  $\gamma'$  precipitates size

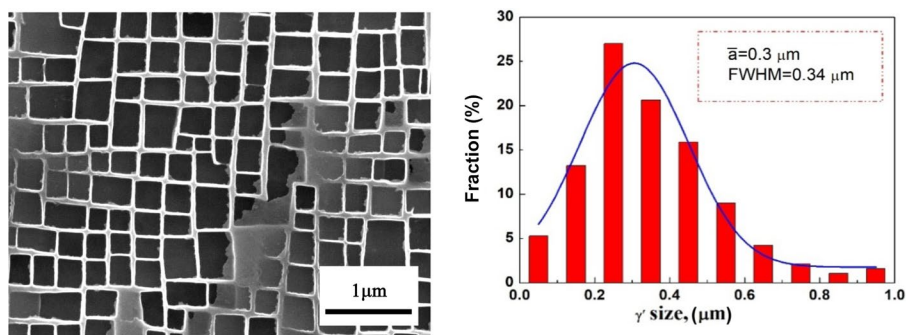
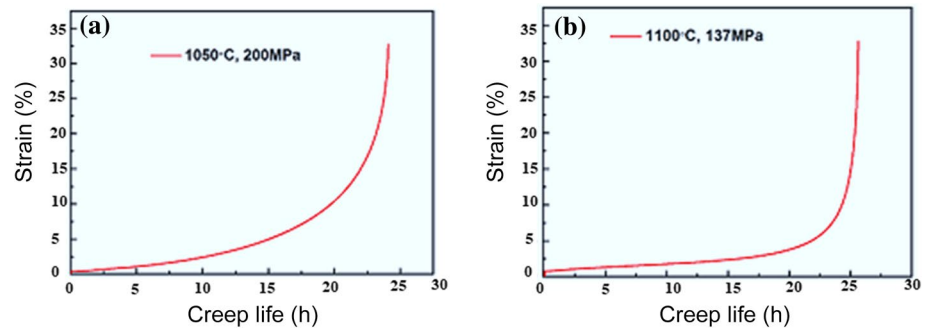


**Fig. 2** High temperature and low stress creep curves of the experimental SX superalloy at 1050 °C/200 MPa **a** and 1100 °C/137 MPa **b**



the conditions of 1050 °C/200 MPa and 1100 °C/137 MPa, respectively. The LD experimental alloy exhibits nearly the same creep life although the temperature and stress are different. In other words, under current creep conditions, rising temperature of 50 °C plays nearly the same role as decreasing stress of 63 MPa, the detailed relationship will be discussed in the following sections. It can be seen that the initial creep stage of the alloy is very short under both conditions, and the alloy has begun to transform from the first stage to the steady stage after 0.5 h creep test. In contrast, the steady-state creep rate of the alloy at 1100 °C/137 MPa is lower than at 1050 °C/200 MPa.

### 3.3 $\gamma/\gamma'$ Morphologies After Creep Failure

Under the combined effect of temperature and stress, the microstructure of nickel-based single crystal superalloy will change obviously, such as,  $\gamma'$  phase rafting and dislocation networks form at the  $\gamma/\gamma'$  interface. The rafting phenomenon of single crystal superalloy at high temperature and low stress creep is inevitable because the  $\gamma/\gamma'$  microstructure is under a metastable state. The driving force of  $\gamma'$  rafting is

mainly due to the existence of misfit internal stress between the  $\gamma$  matrix and  $\gamma'$  phase, as well as the applied stress. Simultaneously, the increase of diffusion coefficient of alloy elements caused by high temperature further promotes the occurrence of rafting. For the experimental alloy studied in this work, the total contain of refractory elements is about 11 wt%, thus, the rafting rate might be higher than other second-generation alloys.

As the grain boundary in nickel-based single crystal superalloy is eliminated, the evolution of  $\gamma'$  precipitates becomes the main influencing factor for the mechanical properties. Therefore, the  $\gamma/\gamma'$  morphologies of the alloy after creep fracture under two conditions is carefully observed, as shown in Fig. 3a (1050 °C/200 MPa) and Fig. 3b (1100 °C/137 MPa). Clearly, the regular rafting microstructures has formed under both conditions.

The average thickness (perpendicular to the direction of the stress axis) of the  $\gamma'$  precipitates after creep is about 0.7  $\mu\text{m}$  and 1  $\mu\text{m}$  at 1050 °C/200 MPa and 1100 °C/137 MPa, respectively. In addition, the rafting direction of the alloy is perpendicular to the direction of the stress axis, which indicates that the lattice misfit between the  $\gamma/\gamma'$  precipitate of

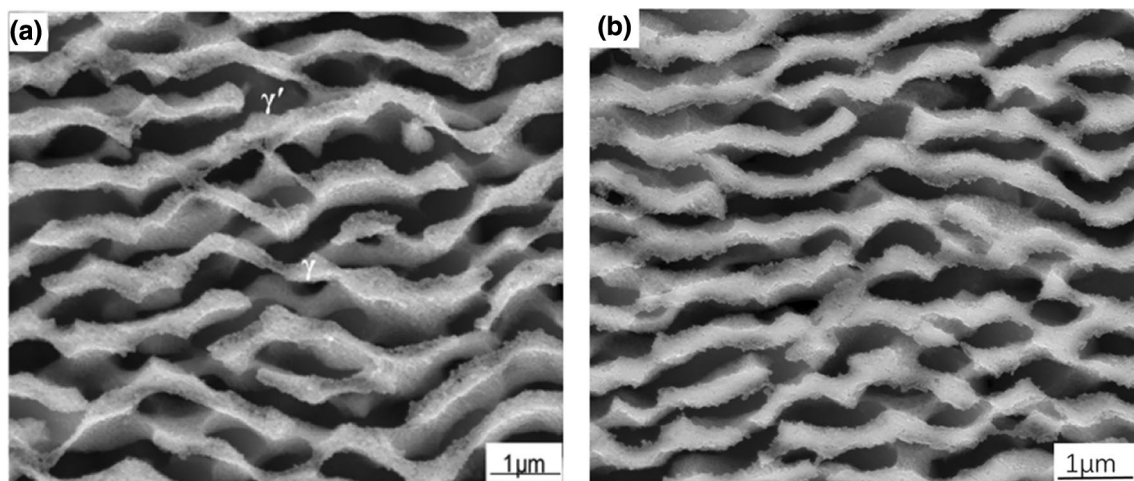


**Fig. 3** SEM pictures of the rafting  $\gamma/\gamma'$  morphologies of the experimental SX superalloy after creep failure at high temperature and low stress **a** 1050 °C/200 MPa, **b** 1100 °C/137 MPa

the alloy at high temperature is negative. It should be noted that although the creep life of the experimental alloy is about 25 h under the two stress conditions selected in this study, the so-called topological inversion of the alloy appeared after creep fracture. The phenomenon of topological inversion refers to the gradual evolution of the  $\gamma'$  precipitates that gradually connected with each other and the  $\gamma$  matrix phase are surrounded by the  $\gamma'$  precipitates.

According to the previous research work of Fredholm and Caron et al. [18, 19], the topological inversion phenomenon is described by the connected number  $N_A(\gamma')$  of gamma-prime precipitates to quantitatively characterize the microstructure evolution of the two phases and determine whether the topological inversion has occurred. The specific formula used to describe the phenomenon of topological inversion is given as follow:

$$N_A(\gamma') = (N_T - N_{TP})/2S$$

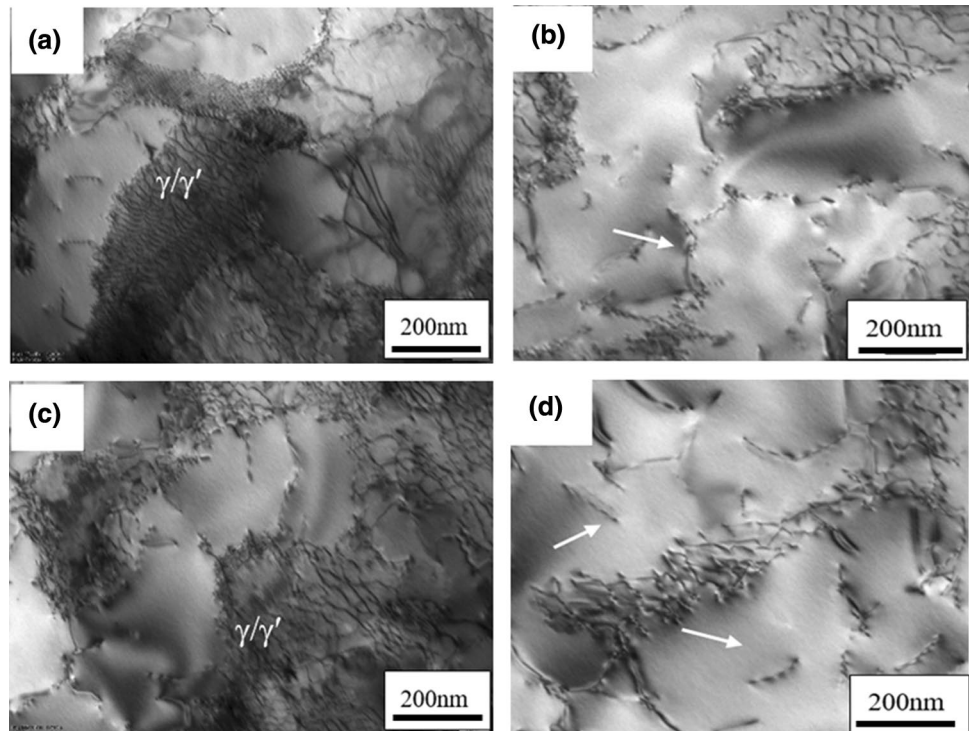
here,  $N_{TP}$  and  $N_T$  refer to the number of bifurcation and terminal of  $\gamma'$  precipitates, respectively.  $S$  represents the area which is analyzed. It can be seen that the  $N_A(\gamma')$  value after the complete heat-treatment is the number of  $\gamma'$  precipitates in the unit area, and the  $N_A(\gamma')$  is positive. During the topological inversion occurs, the terminal number  $N_T$  is smaller than the bifurcation number  $N_{TP}$ , thus, the  $N_A(\gamma')$  shows a negative value. After systematic analysis and calculation, the connection number of the alloy after creep rupture under 1050 °C/200 MPa and 1100 °C/137 MPa is

–0.04 and –0.06, respectively. In other words, the topological inversion takes place under the two creep conditions mentioned above. Furthermore, the change of temperature and stress have little influence on appearance of topological inversion. Topological inversion occurs, namely  $\gamma'$  interconnected enclosure  $\gamma$ , had affected the creep mechanism and creep properties of the alloy.

### 3.4 Dislocation Configurations After Creep Failure

Figure 4 shows the dislocation configurations of the experimental SX superalloys after creep failure under 1050 °C/200 MPa (Fig. 4a and b) and 1100 °C/137 MPa (Fig. 4c and d). It is well known that the denser dislocation network can effectively hinder the matrix dislocations shearing into the  $\gamma'$  precipitates thus, it is of vital importance for maintaining a low minimum creep rate and longer creep life. Clearly, the dislocation networks at the rafting  $\gamma/\gamma'$  interface has formed under both creep conditions, however, the dislocation networks under the two conditions are not denser compared to other generation Ni-based SX superalloys [20–24]. Consequently, the hinder effect caused by dislocation networks is negligible, and a number of superdislocations shearing into the rafting  $\gamma'$  precipitates under both creep conditions (Fig. 4b and d) are observed. These shearing events are more common as creep strain accumulated in the deformed  $\gamma$  matrix in the tertiary stage [25]. The processes of matrix dislocations shearing into the rafted gamma-prime precipitates have a great contribution to the

**Fig. 4** TEM picture of dislocation configurations of the experimental SX superalloy after creep failure at 1050 °C/200 MPa (a, b) and 1100 °C/137 MPa (c, d). Beam = [001]



rapid failure of the experimental alloys. Another conclusion can be drawn that although the test temperature and loading stress is obviously different, the deformation mechanisms are nearly the same.

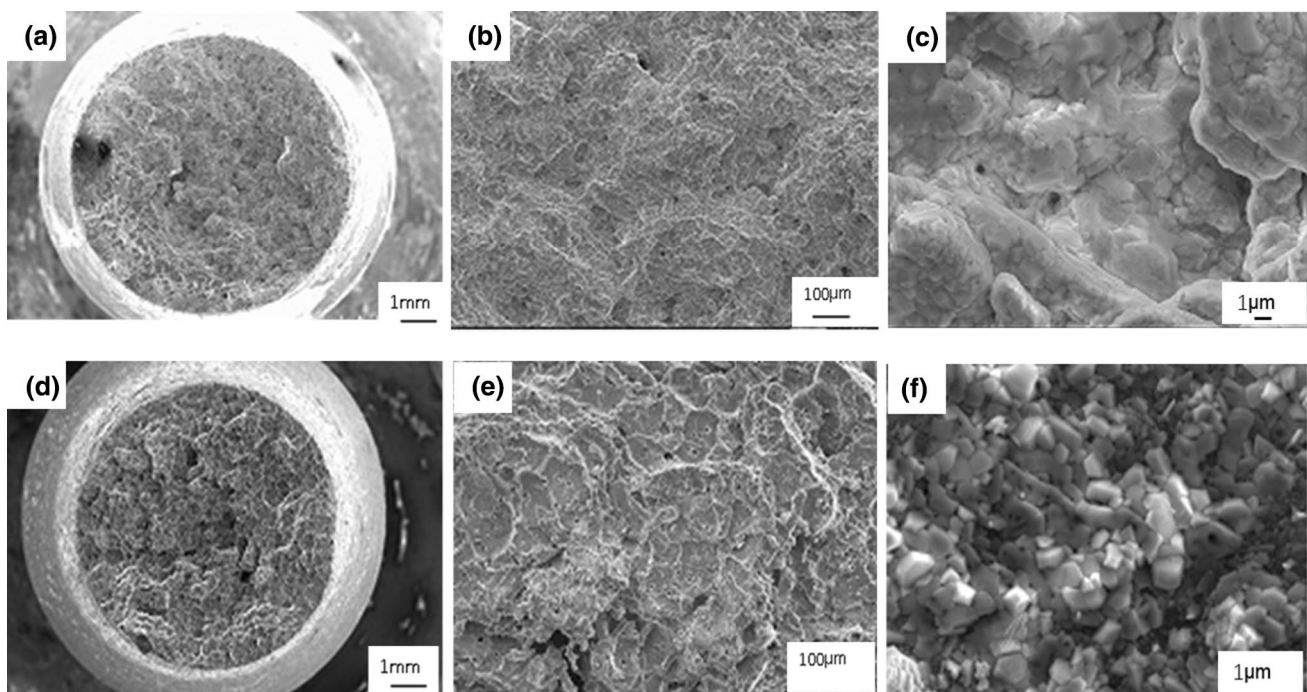
### 3.5 Fracture Characteristics

Figure 5 shows the fracture morphologies of the experimental alloy after creep deformation under 1050 °C/200 MPa (a–c) and 1100 °C/137 MPa (d–f). The nicking phenomenon was observed in the experiment alloy under two kinds of high temperature and low stress conditions. In addition, the fracture features were both identified to be micro-void coalescence fracture. The vacancy gradually accumulated and formed micro-pores during the high-temperature creep process. Driven by the applied stress, stress concentration begins to accumulate at the edge of the micro-pores. When the stress is high enough, the micro-cracks firstly formed at the edge of the pores and then slowly expanded by the stress. As shown in Fig. 5b and e, the micro-cracks formed at the edge of each micro-pore and continuously expanded. When the adjacent cracks met with each other, an edge would be generated. At this time, the micro-cracks had converged to form a larger micro-crack. After the propagation of micro-cracks, the relatively smooth areas were left. When the different micro-crack propagation encountered, some white-bright lines could be clearly observed, as shown in Fig. 5b and f. Actually, it is a slow process for the accumulation of

vacancy to form creep holes as well as the propagation of micro-cracks, which mainly occur in the early and middle stages of steady state creep. As the increasing micro-cracks had accumulated to form the main crack, the crack propagation speed was promoted significantly. Subsequently, the alloy plastic deformation intensified, the obvious shrinkage was observed, and the creep process of the alloy came to the third stage of creep, namely the accelerated fracture stage. Figure 5c and f displayed the local enlarged images of the fracture surface of the alloy, from which the presence of oxidation products can be clearly observed. In fact, in the later stage of creep process, once the macroscopic crack is formed, the top regions of crack will be oxidized, thus the hard and brittle oxide may further promote the crack propagation behavior, hence the alloy can come to the fracture failure in the next several hours.

### 3.6 Effect of Temperatures and Stresses on Creep Life

Since the diffusion rate of elements is influenced by temperature, the effect of temperature on the rafting rate of alloys is of great significance [26, 27]. However, in the process of creep deformation at high temperature, the applied stress and temperature maybe influenced by each other. There was no significant difference in the creep properties and micro-structure after the alloy fracture under the two conditions, indicating that a small decrease in temperature has limited



**Fig. 5** Fracture morphology of the experimental SX superalloy after 1050 °C/200 MPa a–c and 1100 °C/137 MPa d–f. a, d Macrofracture, b, c, e, f partial enlargement

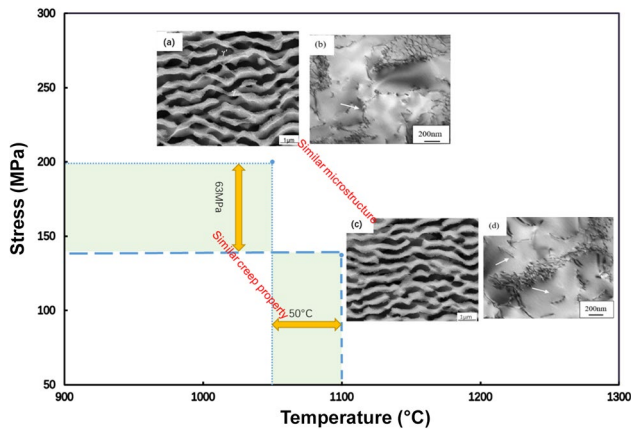


**Fig. 6** The similar creep property was obtained with the decrease of 63 MPa in stress and the increase of 50° in temperature

influence on creep life in the range of high temperature. On the one hand, for the same alloy, the creep behavior of single crystal alloys above 850 °C is not sensitive to the small misorientation. (after reaching the threshold stress). On the other hand, the topological inversion had taken place during the creep fracture process under both conditions, and the deformation mechanism of the dislocation cutting  $\gamma'$  phase was not considerably different. These two aspects have been schematically shown in Fig. 6.

## 4 Conclusions

The creep behavior of a Low density single crystal superalloy at different temperatures and stresses had been studied. The following conclusions could be drawn from this work:

1. The density of experiment alloy was 8.2 g/cm<sup>3</sup>, which was significantly lower than that of other typical second-generation SX superalloys.
2. The  $\gamma'$  precipitates under both conditions had formed a regular raft framework. The average thickness (perpendicular to the direction of the stress axis) of the  $\gamma'$  precipitates after creep were about 0.7  $\mu\text{m}$  and 1  $\mu\text{m}$  at 1050 °C/200 MPa and 1100 °C/137 MPa, respectively.
3. After creep deformation, the so-called topological inversion of the experiment alloy took place under both conditions of 1050 °C/200 MPa and 1100 °C/137 MPa.
4. For the experiment alloy studied in this work, within a certain temperature range from 1050 to 1100 °C, the per unit stress showed nearly the same effect of per unit temperature on the whole creep life.

**Acknowledgements** The financial supports provided by National Natural Science Foundation of China (NSFC) under Grant Nos. 51701210 and 51671188, National Science and Technology Major Project under

Grant No. 2017-VI-0002-0072, National Key R&D Program of China under Grant No. 2017YFA0700704, Youth Innovation Promotion Association, Chinese Academy of Sciences and Innovation Academy for Light-duty Gas Turbine, Chinese Academy of Sciences under Grant No. CXYJJ20-MS-03.

## References

1. Y. Koizumi, T. Kobayashi, H. Harada, T. Yamagata, in *Advances in Turbine Materials, Design and Manufacturing*, ed. by A. Strang. 4th International Charles Parsons Turbine Conference, Newcastle upon Tyne, November 4-6, 1997. (The Institute of Materials, London, 1997), pp. 679–684
2. Z. Huda, P. Edi, *Mater. Des.* **46**, 552–560 (2013)
3. J.X. Zhang, H. Harada, Y. Koizumi, T. Kobayashi, *Acta Mater.* **53**, 4623–4633 (2005)
4. R.C. Reed, T. Tao, N. Warnken, *Acta Mater.* **57**, 5898–5913 (2009)
5. F. Pyczak, B. Devrient, F.C. Neuner, H. Mughrabi, *Acta Mater.* **53**, 3879–3891 (2005)
6. X.G. Wang, J.L. Liu, T. Jin, X.F. Sun, *Mater. Des.* **63**, 286–293 (2014)
7. A. Sato, H. Harada, T. Yokokawa, T. Murakumo, Y. Koizumi, T. Kobayashi, H. Imai, *Scr. Mater.* **54**, 1679–1684 (2006)
8. A.C. Yeh, S. Tin, *Scr. Mater.* **52**, 519–524 (2005)
9. A. Heckl, S. Neumeier, S. Cenanovic, M. Göken, R.F. Singer, *Acta Mater.* **59**, 6563–6573 (2011)
10. Y.S. Huang, X.G. Wang, C.Y. Cui, J.G. Li, L.H. Ye, G.C. Hou, Y.H. Yang, J.L. Liu, J.D. Liu, Y.Z. Zhou, X.F. Sun, *Mater. Sci. Eng. A* **773**, 138886 (2020)
11. F. Liu, G.C. Yang, X.F. Guo, *Mater. Sci. Eng. A* **311**, 54–63 (2001)
12. F. Liu, G.C. Yang, *J. Mater. Sci.* **37**, 2713–2719 (2002)
13. F. Liu, G.C. Yang, *J. Mater. Sci. Lett.* **20**, 987–989 (2001)
14. G. Eggeler, A. Dlouhy, *Acta Mater.* **45**, 4251–4262 (1997)
15. R.C. Reed, *The Superalloys Fundamentals and Applications* (Cambridge University Press, Cambridge, 2006), pp. 16–28
16. A. Sato, H. Harada, A.C. Yeh, K. Kawagishi, T. Kobayashi, Y. Koizumi, T. Yokokawa, J.X. Zhang, *Superalloy* **2008**, 131–138 (2008)
17. X.G. Wang, J.L. Liu, T. Jin, X.F. Sun, Y.Z. Zhou, Z.Q. Hu, J.H. Do, *Mater. Sci. Eng. A* **626**, 406–414 (2015)
18. A. Fredholm, J.L. Strudel, *Superalloys* **1984**, 211–220 (1984)
19. P. Caron, C. Ramusat, F. Diologent, *Superalloys* **2008**, 159–167 (2008)
20. Z.H. Tan, X.G. Wang, L.H. Ye, G.C. Hou, R. Li, Y.H. Yang, J.L. Liu, J.D. Liu, L. Yang, B. Wang, P. Dong, J.G. Li, Y.Z. Zhou, X.F. Sun, *Mater. Sci. Eng. A* **761**, 138042 (2019)
21. W. Song, X.G. Wang, J.G. Li, L.H. Ye, G.C. Hou, Y.H. Yang, J.L. Liu, J.D. Liu, W.L. Pei, Y.Z. Zhou, X.F. Sun, *Mater. Sci. Eng. A* **772**, 138646 (2020)
22. J.X. Zhang, T. Murakumo, Y. Koizumi, T. Kobayashi, H. Harada, S. Masaki, *Metall. Mater. Trans. A* **33**, 3741–3746 (2002)
23. T. Jin, Y.Z. Zhou, X.G. Wang, J.L. Liu, X.F. Sun, Z.Q. Hu, *Acta Metall. Sin.* **51**, 1153 (2015)
24. C. Schulze, M. Feller-kniepmeier, *Mater. Sci. Eng. A* **281**, 204–212 (2000)
25. X.G. Wang, J.L. Liu, T. Jin, X.F. Sun, Z.Q. Hu, J.H. Do, B.G. Choi, I.S. Kim, C.Y. Jo, *Mater. Des.* **67**, 543–551 (2015)
26. M.H. Li, X.F. Sun, W.Y. Hu, H.G. Guan, *Mater. Lett.* **61**, 5169–5172 (2007)
27. T.M. Smith, Y. Rao, Y. Wang, M. Ghazisaeidi, M.J. Mills, *Acta Mater.* **141**, 261–272 (2017)

**Publisher's Note** Springer Nature remains neutral with regard to jurisdictional claims in published maps and institutional affiliations.